



Thermomechanical modelling of slab detachment

Taras V. Gerya^{a,b,*}, David A. Yuen^c, Walter V. Maresch^d

^a*Geologisches Institut, ETH, Zürich, CH-8092 Zurich, Switzerland*

^b*Institute of Experimental Mineralogy, Russian Academy of Sciences, 142432 Chernogolovka, Moscow, Russia*

^c*University of Minnesota Supercomputing Institute and Department of Geology and Geophysics, University of Minnesota, Minneapolis, Minnesota 55455-0219, USA*

^d*Institut für Geologie, Mineralogie und Geophysik, Ruhr-Universität Bochum, 44780 Bochum, Germany*

Received 20 November 2003; received in revised form 8 July 2004; accepted 19 July 2004

Editor: R.D. van der Hilst

Abstract

Slab detachment or breakoff is appreciated as an important geological process, as shown by recent tomographic imaging. Using a 2-D upper-mantle model 660-km deep and 2000-km wide, we have investigated with a 2-D finite-difference and marker-in-cell numerical technique the multi-resolutional character of the thermomechanical phenomena related to this complex geological process. Our experiments show that this process can be initiated in form of slab necking by a prolonged (8–30 My) period of slab weakening due to thermal diffusion (<20 °C/My) after cessation of active subduction. The rapid detachment process takes place over a few million years and is accelerated by non-Newtonian strain-rate softening and focused thermal erosion (>60 °C/My) due to strong positive thermal feedback from shear heating. Detached slab fragments sink rapidly with a tendency for coherent rotation. The influence of temperature- and pressure-dependent thermal conductivity on the process of thermal weakening of the slab is quite significant. This supports the idea that the breakoff process is triggered by thermal diffusion on a time scale linearly dependent on heat conductivity. Rapid topographic changes and increasing volcanic activities due to the melting of subducted oceanic crust are possible scenarios of this vigorously driven geodynamic process.

© 2004 Elsevier B.V. All rights reserved.

Keywords: slab breakoff; subduction zones; dynamic topography; shear heating

1. Introduction

Slab detachment or slab breakoff is a realistic geological process originally inferred seismically from gaps in the hypocentral distributions associated with subducted slabs (e.g., [1]) and supported by both theoretical considerations [2–4] and seismic tomog-

* Corresponding author. Tel.: +41 1 6322336; fax: +41 1 6321030.

E-mail address: taras.gerya@erdw.ethz.ch (T.V. Gerya).

raphy studies [5–8]. This process can involve mantle lithosphere of continental (e.g., [9]), oceanic (e.g., [7]) or continental margin (e.g., [4,10–12]) origin. Slab detachment is commonly suggested to be associated with the early stages of continental collision (e.g., [4,13]), due to a decrease in the subduction rate damped by the positive buoyancy of continental lithosphere introduced into the subduction region. Slab detachment and slab fragmentation may also be induced by a decrease in subduction rate in other geodynamic settings. This process can thus play an influential role along slab edges (e.g., [7]).

In spite of past significant progress in our understanding of slab detachment from both analytical and numerical studies (e.g., [4,9,13–18]), there have been no studies on the dynamics of this process with a realistic rheological–petrological model to account for the effects of slab melting, as well as adiabatic and shear heating (e.g., [17,19]). Most previous studies have used a static situation with simplified rheological models (e.g., [4,13,14,18]). The dynamic modeling presented by Pysklywec et al. [9] and Houseman and Gubbins [16], which considered different modes of deformation of subducting lithosphere, is also based on a simplified rheology, and does not account for thermal effects such as thermal diffusion and shear heating, which, as we will demonstrate, turn out to be extremely important.

In this paper, we will investigate, by means of a systematic, high resolution 2-D study, the dynamics of detachment of oceanic slabs due to thermal diffusion after cessation of active subduction. Our primary goal is to study the dynamics, geometry and modes of slab detachment, and to take into account the effects of

pressure-, temperature-, and strain-rate-dependent rheology of the mantle and oceanic crust, of pressure- and temperature-dependent thermal conductivity (Table 1), and of shear and adiabatic heating as well as partial melting of the oceanic crust.

2. Initial and boundary conditions of the 2-D model

Fig. 1 displays our 2-D numerical model, which is specifically designed for studying dynamic processes in a subducted slab after cessation of active subduction. A nonuniform rectangular grid with variable 2–10-km resolution is designed in such a way as to provide the highest resolution of 2×2 km in the upper central, 400-km-wide and 200-km-deep area of the model (Fig. 1a), where the detachment process is expected to be localized. The initial thermal structure of subducted slab is defined by the following two parameters (Fig. 1b): (i) a given constant longitudinal temperature gradient along the 450-km-long upper interface of the slab starting from 0°C at the surface, and (ii) effective uniform slab thickness limited by the 1300°C isotherm at the bottom. Initial temperature distribution across the slab is taken to be linear. Taking into account that the thermal structures of subducting slabs depend on many physical parameters (slab age, subduction rate and its variations through time, shear and adiabatic heating, etc.), our simple formalization allows general applicability of the modeling results independent of slab prehistory. Indeed, the rough correspondence of our simple slab parameterization with slab age and previous subduction rate can be established (Table 2) by comparing

Table 1
Material properties^a used in 2-D numerical experiments

Material	ρ_0 , kg/m ⁻³	k , W/m K	T_{solidus} , K	T_{liquidus} , K	H_L , kJ/kg ⁻¹	H_V , $\mu\text{W/m}^{-3}$
Oceanic crust (solid), 2900 (molten)	3200–3500	$[1.18+474/(T_K+77)] \times \exp(0.00004P_{\text{MPa}})$	$973-70400/(P+354)+77800000/(P+354)^2$ at $P < 1600$ MPa, $935+0.0035P+0.0000062P^2$ at $P > 1600$ MPa	$1423+0.105P$	380	0.25
Mantle (lithospheric and asthenospheric)	3300	$[0.73+1293/(T_K+77)] \times \exp(0.00004P_{\text{MPa}})$	–	–	–	0.022
References	[20,21]	[22]	[23]	[23]	[20,21]	[20]

^a $C_p=1000$ J/kg, $\alpha=3 \times 10^{-5}$ K⁻¹, $\beta=1 \times 10^{-5}$ MPa⁻¹ for all types of rocks.

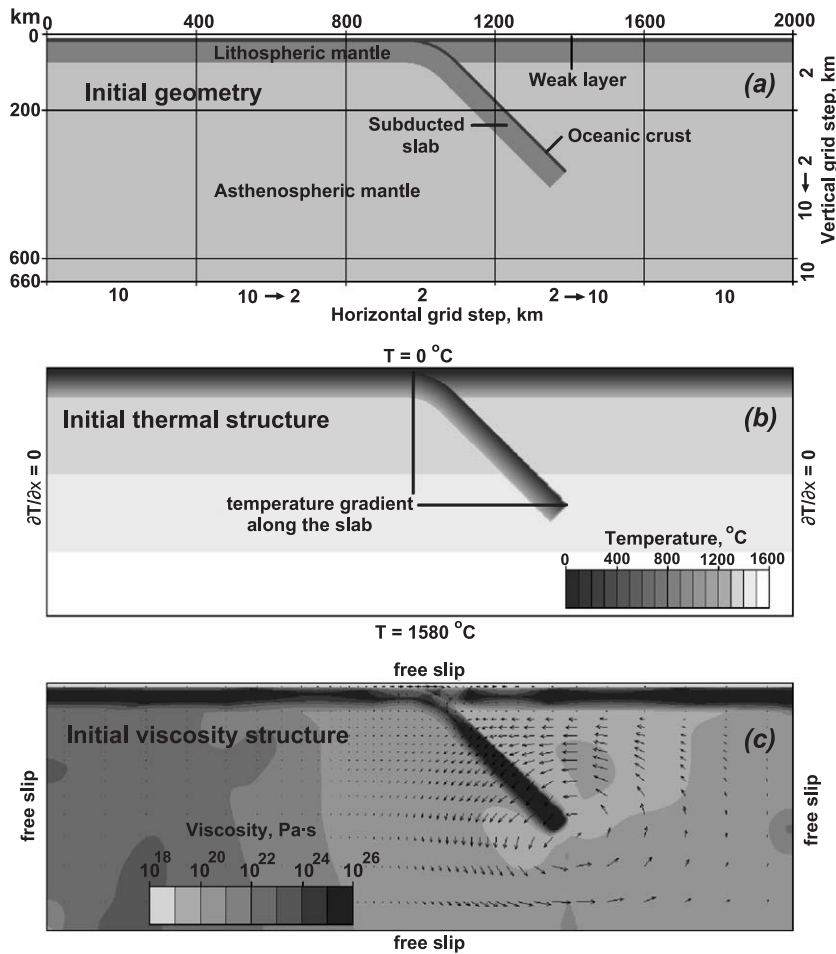


Fig. 1. Design of 2-D numerical model used in this study: (a) initial distribution of different rock types and geometry of numerical grid, (b) initial thermal structure and boundary conditions, (c) initial calculated dynamic viscosity structure and mechanical boundary conditions. The lithospheric and asthenospheric mantles shown in different grey scales do not differ in physical properties; the discrimination between them is used only for a better representation of slab deformation and model geometry development. Arrows in (c) show calculated initial flow pattern corresponding to slab bending. See text for details.

initial thermal structure with well known slab thermal models (e.g., [24,27]).

Thermal boundary conditions (Fig. 1b) correspond to 0 °C at the upper and 1580 °C at the lower boundary; a zero flux condition for the horizontal heat flow is imposed at the vertical boundaries. The velocity boundary conditions (Fig. 1c) are reflective at all boundaries. The dynamic viscosity structure shown in Fig. 1c corresponds to the given temperature distribution (Fig. 1b), and characterizes the velocity field associated with the bending of the slab at the initial stage of the numerical experiments. As shown

from both geophysical studies (e.g., [5,8]) and numerical modeling (e.g., [18]), slab detachment exerts a major effect on the topographic evolution of the adjacent region. Our model, therefore, includes in a simplified way the possibility for surface movements. The top surface is calculated dynamically at each time step as a free surface (e.g., [28]). To account for the changes in the topography, we have used a layer with a lower viscosity (10^{18} Pa s), whose initial thickness is 8 km on the top of the oceanic crust (Fig. 1a). The density of this layer is taken to be either 1 kg m^{-3} (air) or 1000 kg m^{-3} (sea water) for different numerical

Table 2
Parameters of selected numerical experiments

Model	Weak layer	Slab thickness, km (model slab age, ^a My)	Longitudinal temperature gradient along the slab, °C/km (model subduction rate, ^b cm/a)		Shear heating	Melting of the oceanic crust	Mantle: flow law/ $\Delta V/\lambda$	Oceanic crust: flow law/ $\Delta V/\lambda/\rho_0$	Time (My)/depth (km) of slab detachment
			0–150 km	150–450 km					
1 (deab)	water	65 (30)	0	0 (>22)	included	included	O1 (dry)/8/0.5	PI (An ₇₅)/0/0.95/3200	22.7/150
2 (deac)	water	65 (30)	0	0 (>22)	included	included	O1 (dry)/0/0.5	PI (An ₇₅)/0/0.95/3200	13.7/280
3 (deae)	water	65 (30)	0	0 (>22)	included	not included	O1 (dry)/8/0.5	PI (An ₇₅)/0/0.95/3200	21.3/146
4 (deaf)	water	65 (30)	0	0 (>22)	included	included	O1 (dry)/16/0.5	PI (An ₇₅)/0/0.95/3200	no breakoff
5 (deag)	water	65 (30)	0	0 (>22)	not included	included	O1 (dry)/8/0.5	PI (An ₇₅)/0/0.95/3200	24.6/160
6 (deah)	water	65 (30)	0	2.7 (1.2)	included	included	O1 (dry)/8/0.5	PI (An ₇₅)/0/0.95/3200	24.8/296
7 (deai)	water	65 (30)	0	1.3 (3.2)	not included	included	O1 (dry)/8/0.5	PI (An ₇₅)/0/0.95/3200	23.7/248
8 (deaj)	water	65 (30)	0	2.7 (1.2)	included	included	O1 (dry)/8/0.5	PI (An ₇₅)/0/0.95/3200	24.1/292, 80/196
9 (deak)	water	65 (30)	0	2.7 (1.2)	included	included	O1 (dry)/8/0.5	PI (An ₇₅)/0/0.95/3500	12.4/408, 19.8/278
10 (deal)	water	65 (30)	0	1.3 (3.2)	included	included	O1 (dry)/8/0	PI (An ₇₅)/8/0.95/3500	17.2/220
11 (deam)	water	65 (30)	0	2.7 (1.2)	included	included	O1 (dry)/8/0	PI (An ₇₅)/8/0.95/3500	13.0/394, 20.1/268
12 (dean)	water	65 (30)	0	1.3 (3.2)	included	not included	O1 (dry)/8/0	PI (An ₇₅)/8/0.95/3500	16.8/158
13 (deao)	water	65 (30)	0	1.3 (3.2)	included	included	O1 (dry)/8/0–0.8 ^c	PI (An ₇₅)/8/0.95/3300	20.7/228
14 (deap)	air	65 (30)	0	1.3 (3.2)	included	included	O1 (dry)/8/0–0.8 ^c	PI (An ₇₅)/8/0.95/3300	20.6/232
15 (deaq)	air	65 (30)	0	1.3 (3.2)	included	included	O1 (dry)/8/0	PI (An ₇₅)/8/0.95/3300	20.6/230
16 (dear)	air	45 (15)	0	1.3 (7)	included	included	O1 (dry)/8/0	PI (An ₇₅)/8/0.95/3300	11.1/230
17 (deas)	air	85 (50)	0	1.3 (1.9)	included	included	O1 (dry)/8/0	PI (An ₇₅)/8/0.95/3300	33.2/222
18 (deat)	air	65 (30)	0.7	0.7 (6)	included	included	O1 (dry)/8/0	PI (An ₇₅)/8/0.95/3300	17.8/150
19 (deau)	air	65 (30)	1.3	1.3 (3.2)	included	included	O1 (dry)/8/0	PI (An ₇₅)/8/0.95/3300	14.5/242
20 (deav)	air	65 (30)	2.0	2.0 (1.7)	included	included	O1 (dry)/8/0	PI (An ₇₅)/8/0.95/3300	11.1/262, 36.5/160
21 (deaw)	air	45 (15)	0	0 (>44)	included	included	O1 (dry)/8/0	PI (An ₇₅)/8/0.95/3300	10.5/108
22 (deax)	air	45 (15)	0.7	0.7 (12)	included	included	O1 (dry)/8/0	PI (An ₇₅)/8/0.95/3300	9.3/112
23 (deay)	air	45 (15)	1.3	1.3 (7)	included	included	O1 (dry)/8/0	PI (An ₇₅)/8/0.95/3300	8.4/258, 29.5/150
24 (deaz)	air	45 (15)	2.0	2.0 (3.4)	included	included	O1 (dry)/8/0	PI (An ₇₅)/8/0.95/3300	7.8/242, 36/148
25 (deba)	air	85 (50)	0	0 (>14)	included	included	O1 (dry)/8/0	PI (An ₇₅)/8/0.95/3300	35.9/188
26 (debb)	air	85 (50)	0.7	0.7 (3.6)	included	included	O1 (dry)/8/0	PI (An ₇₅)/8/0.95/3300	29.0/190
27 (debc)	air	85 (50)	1.3	1.3 (1.9)	included	included	O1 (dry)/8/0	PI (An ₇₅)/8/0.95/3300	22.7/240
28 (debd)	air	85 (50)	2.0	2.0 (1.0)	included	included	O1 (dry)/8/0	PI (An ₇₅)/8/0.95/3300	16.4/292, 43/206
29 (debe)	air	65 (30)	0	0 (>22)	included	included	O1 (dry)/8/0	PI (An ₇₅)/8/0.95/3300	21.0/148
30 (debf) ^d	air	65 (30)	0	0 (>22)	included	included	O1 (dry)/8/0	PI (An ₇₅)/8/0.95/3300	18.1/148
31 (deab)	air	65 (30)	0	0 (>22)	included	included	O1 (dry)/8/0.8	PI (An ₇₅)/8/0.95/3300	unstable slab ^e

^a Model slab age is approximated by comparison with half-space cooling model (e.g. [20]).

^b Model subduction rate is inferred by comparison with the slab thermal model studied by McKenzie [24].

^c Different λ were assumed at different bulk strain (e.g. [9]): $\lambda=0$ when strain<0.5, $\lambda=0-0.8$ when strain=0.5–1.5, $\lambda=0.8$ when strain >1.5.

^d Thermal conductivity of all rocks is increased by 20%.

^e Breakoff occurs immediately below the free surface both to the left (at 0.3 My) and to the right (at 1.6 My) of the slab that is associated with rapid slab sinking and opening of large (~300-km wide) window in the lithosphere substituted by asthenospheric mantle (e.g. [19,25,26]).

experiments. The interface between this layer and the top of the oceanic crust is treated as a free surface [28].

3. Model for partial melting

Melting of subducted oceanic crust to produce characteristic melts is an important process at slab edges formed during slab detachment (e.g., [7,29]). We adopt a model [28] that allows for melting of subducted oceanic crust in the P – T region between the wet solidus and dry liquidus of basalt (Table 1). As a first approximation, the degree of melting is assumed to increase linearly with the temperature according to the relations

$$\begin{aligned} M &= 0 \text{ at } T < T_{\text{solidus}}, \\ M &= (T - T_{\text{solidus}}) / (T_{\text{liquidus}} - T_{\text{solidus}}) \\ &\text{at } T_{\text{solidus}} < T < T_{\text{liquidus}}, \quad M = 1 \text{ at } T > T_{\text{liquidus}}, \end{aligned} \quad (1)$$

where M is the volumetric fraction of melt as a function of temperature; T_{solidus} and T_{liquidus} are, respectively, the wet solidus and dry liquidus temperature of basalt (Table 1).

An effective density, ρ_{eff} , of partially molten rocks is calculated from the formula

$$\rho_{\text{eff}} = \rho_{\text{solid}} - M(\rho_{\text{solid}} - \rho_{\text{molten}}), \quad (2)$$

where ρ_{solid} and ρ_{molten} are, respectively, the densities of solid and molten rock, varying with pressure and temperature according to the relation

$$\rho_{P,T} = \rho_0 [1 - \alpha(T - T_0)] \times [1 + \beta(P - P_0)], \quad (3)$$

where ρ_0 is the standard density at $P_0=0.1$ MPa and $T_0=298$ K; α and β are, respectively, the thermal expansion and compressibility coefficients. We used the variations in the standard density, ρ_0 , of the oceanic crust (3200–3500 kg m⁻³, Tables 1 and 2) to study the possible influence of eclogitization of the oceanic crust [23,30] for the detachment process.

The effects of latent heating are accounted for by an increased effective heat capacity of the partially molten rocks ($C_{p,\text{eff}}$), calculated according to the equation

$$C_{p,\text{eff}} = C_p + H_L / (T_{\text{liquidus}} - T_{\text{solidus}}), \quad (4)$$

where C_p and H_L are, respectively, the isobaric heat capacity and the latent heat of melting of the oceanic crust (Table 1).

4. Rheological model

The viscosity for viscous flow in the upper mantle depends primarily on the strain-rate and the temperature and is given in terms of the second invariant of the deviatoric strain-rate tensors [31] by

$$\eta_{\text{creep}} = (\varepsilon_{\text{II}})^{(1-n)/2n} F(A_D)^{-1/n} \exp[(E + P\Delta V)/nRT], \quad (5)$$

where $\varepsilon_{\text{II}}=(1/2)\varepsilon_{ij}\varepsilon_{ij}$ is the second invariant of the strain rate tensor, with dimension s⁻²; E is the activation energy in kJ mol⁻¹; ΔV is the activation volume, J MPa⁻¹ mol⁻¹; A_D is the material constant in Pa^{- n} s⁻¹, n is the stress exponent; and R is the gas constant. F is a dimensionless coefficient depending on the type of experiments on which the flow law is based (e.g., $F=2^{(1-n)/n}/3^{(1+n)/2n}$ for triaxial compression and $F=2^{(1-2n)/n}$ for simple shear).

For representing the ductile rheology of different rocks, we used flow laws for dislocation creep of experimentally studied geomaterials (Table 2). Flow law parameters for Eq. (5) of these materials are taken from the compilation of Ranalli [31]:

- oceanic crust—flow law of plagioclase with composition An₇₅, with $E=238$ kJ mol⁻¹, $n=3.2$, and $\log A_D=-3.5$ (A_D given in MPa^{- n} s⁻¹), $\Delta V=0-8$ J MPa⁻¹ mol⁻¹;
- mantle rocks (both lithospheric and asthenospheric)—flow law of dry olivine, with $E=532$ kJ mol⁻¹, $n=3.5$, and $\log A_D=4.4$ (A_D given in MPa^{- n} s⁻¹), $\Delta V=0-16$ J MPa⁻¹ mol⁻¹.

We used different values of the effective activation volume ΔV to test the influence of this parameter on the regime of detachment. Significant variations in the effective activation volume representing the dependence of activation energy on pressure may be related to the variation in fugacity of water

strongly affecting rheological properties of mantle rocks (e.g., [32]).

At temperatures lower than about 700 K, the ductile rheology for solid rocks ($M < 0.1$) is combined with a quasi-brittle rheology to yield an effective rheology [25]. For this purpose the Mohr–Coulomb law (e.g., [31,33]) is simplified to the yield stress, σ_{yield} , criterion and implemented by a limiting of creep viscosity, η_{creep} , as follows

$$\eta_{\text{creep}} \leq \sigma_{\text{yield}} / (4\varepsilon_{\text{II}})^{1/2}, \quad \sigma_{\text{yield}} = (M_1 P_{\text{lith}} + M_2)(1 - \lambda) \quad (6)$$

where $\lambda = P_{\text{fluid}}/P_{\text{lith}}$ is the pore fluid pressure coefficient, i.e., the ratio between pore fluid pressure, P_{fluid} , and lithostatic pressure, P_{lith} ; M_1 and M_2 are empirical constants [33]. We explored significant variations in the pore pressure coefficient λ for mantle rocks (Table 2) in order to study the influence of brittle strength of the lithosphere.

The effective viscosity, η , of molten rocks ($M > 0.1$) was taken constant (10^{18} Pa s). As the lower and upper cut values for viscosity of all types of rocks in our numerical experiments, we used 10^{18} and 10^{26} Pa s, respectively.

5. Conservation equations and numerical implementation

We have considered two-dimensional creeping flow wherein both thermal and chemical buoyant forces are included. The conservation of mass is approximated by the incompressible continuity equation

$$\partial v_x / \partial x + \partial v_z / \partial z = 0. \quad (7)$$

The 2-D Stokes equations for creeping flow take the form:

$$\partial \sigma_{xx} / \partial x + \partial \sigma_{xz} / \partial z = \partial P / \partial x \quad (8)$$

$$\partial \sigma_{zz} / \partial z + \partial \sigma_{xz} / \partial x = \partial P / \partial z - g\rho(T, C, M). \quad (9)$$

The density $\rho(T, C, M)$ depends explicitly on the temperature, the composition, and the degree of melting (see Section 3).

We also employ viscous rheological constitutive relationships between the stress and strain rate, whose coefficient η represents the effective viscosity, which depends on the composition, temperature, pressure, strain rate and degree of melting (see Section 4)

$$\sigma_{xx} = 2\eta\varepsilon_{xx}, \quad \sigma_{xz} = 2\eta\varepsilon_{xz}, \quad \sigma_{zz} = 2\eta\varepsilon_{zz}, \quad \varepsilon_{xx} = \partial v_x / \partial x, \\ \varepsilon_{xz} = \frac{1}{2}(\partial v_x / \partial z + \partial v_z / \partial x), \quad \varepsilon_{zz} = \partial v_z / \partial z.$$

We have adopted [34] a Lagrangian frame of reference in which the temperature equation with a pressure- and temperature-dependent thermal conductivity $k(T, P)$ [35] takes the form.

$$\rho C_p (DT/Dt) = \partial q_x / \partial x + \partial q_z / \partial z + H_r + H_a + H_s, \\ q_x = k(T, P)(\partial T / \partial x), \quad q_z = k(T, P)(\partial T / \partial z), \\ H_r = \text{constant}, \quad H_a = T\alpha[v_x(\partial P / \partial x) + v_z(\partial P / \partial z)] \\ \approx T\alpha\rho v_z g, \quad H_s = \sigma_{xx}\varepsilon_{xx} + \sigma_{zz}\varepsilon_{zz} + 2\sigma_{xz}\varepsilon_{xz}, \quad (10)$$

where DT/Dt represents the substantive time derivative. We would like to emphasize here the presence of both shear and adiabatic heating terms in our temperature equation, which plausibly have significant effects on the detachment process (e.g., [17,19]), and which have not been studied so far.

The notations in Eqs. (8)–(10) are: x and z denote, respectively, the horizontal and vertical coordinates, in m; v_x and v_z are components of velocity vector v in m s^{-1} ; t is time in s; σ_{xx} , σ_{xz} , σ_{zz} are components of the viscous deviatoric stress tensor in Pa; ε_{xx} , ε_{xz} , ε_{zz} are components of the strain rate tensor in s^{-1} ; P the pressure in Pa; T the temperature in K; q_x and q_z are heat fluxes in W m^{-2} ; η the effective viscosity in Pa s; ρ the density in kg m^{-3} ; $g = 9.81 \text{ m s}^{-2}$ is the gravitational acceleration; k is the thermal conductivity in $\text{W m}^{-1} \text{K}^{-1}$; C_p is the isobaric heat capacity in $\text{J kg}^{-1} \text{K}^{-1}$; H_r , H_a , and H_s denote, respectively, radioactive, adiabatic and shear heat production in W m^{-3} .

We have employed the recently developed 2-D code I2VIS [34], based on finite-differences with a marker-in-cell technique, which allows for the accurate conservative solution of the governing equations on a rectangular fully staggered Eulerian grid for multiphase flow.

6. Results from numerical experiments

We have garnered results from well over 50 different numerical models (see description of selected representative runs in Table 2). These simulations have been calculated over a finite-difference grid with 441×187 irregularly spaced Eulerian points (Fig. 1a). In contrast to our recent high-resolution numerical study of multiscale dynamics of hydrous cold plumes at subduction zones [36], simplified lithological structure of our model (Fig. 1a) allowed us to use a moderate number of markers (~5 million) for portraying the details of the temperature, material and viscosity fields. Lateral viscosity contrasts, up to 10^8 , are maintained in all of the models shown here.

Figs. 2–4 show different aspects of development for our first reference model involving a descending cold slab (Model 1 in Table 2). The detachment process starts after prolonged period (~20 My) of thermal diffusion of the slab in the form of a rapid (within less than 2 My) extensional necking process (e.g., [16]) localized at a relatively shallow 150-km depth (Fig. 2, 22.7 My) and driven by the negative buoyancy of the slab. Since the brittle strength of mantle rock in this experiment is assumed to be high, the necking process proceeds in the ductile regime by power-law rheology. The detached slab sinks toward the bottom of the upper mantle with a strong tendency for coherent rotation at the reflective lower boundary of the model (Fig. 2, 22.8–23.2 My). The slab velocity can reach up to 1 m per year. Furthermore, the falling slab is lubricated by localized zones of lowered viscosity and shear heating in the surrounding mantle. The amount of shear heating ($>20 \mu\text{W m}^{-3}$) produced in these zones (Fig. 3, 22.7–23.2 My) surpasses the amount of heat produced by radioactive elements in the mantle by a factor of $>10^3$. Shear heating exerts a significant influence on the dynamics of the detachment process: slab breakoff develops 8% faster in numerical experiments with viscous dissipation included (cf. Models 1 and 5 in Table 2). As shown by Larsen et al. [37], the significance of shear heating increases with the power-law index n (see Eq. (5)), which emphasizes the importance of using a realistic power-law rheology of mantle. Therefore, the observed rapid slab necking process can be considered as not purely

mechanical. Shear heating is always focusing in the slab necking area (Fig. 3, 22.7 My), facilitating a focused thermal erosion of the slab in this zone. This focusing is clearly reflected by substantive temperature derivative, DT/Dt , field (Fig. 2, 22.7 My, zoomed area in the left column). Effective values of DT/Dt reach $>60 \text{ }^\circ\text{C/My}$, which is much higher than background values related to thermal diffusion within the rest of the slab ($DT/Dt < 20 \text{ }^\circ\text{C/My}$). In models without shear heating, only weak focusing of thermal diffusion occurs ($DT/Dt = 25\text{--}30 \text{ }^\circ\text{C/My}$) due to the advective sharpening of temperature gradients in the necking area. The influence of shear heating is opposite to the influence of partial melting of the oceanic crust, which causes a 2–7% delay in the breakoff process (cf. Models 1 and 3, 10 and 12 in Table 2) due to the consumption of latent heat that slows down thermal diffusion of the slab. Melting occurs within the subducted oceanic crust at the top of the slab at a restricted depth interval of 100 to 200 km (Fig. 2, 14.8–22.8 My) defined by the nonlinear dependence of the wet solidus temperature of the oceanic crust on pressure (Table 1). For the same reason, rapid crystallization of melts occurs in the sinking slab after detachment, though stable melting develops at shallower depths on the edge of upper slab fragment attached to the overriding plate (cf. Fig. 2, 22.7 and 22.8 My).

The coherent behavior of the detached slab is caused by the significant (300–500 $^\circ\text{C}$) negative temperature anomaly in its core, resulting in an increased effective viscosity of the slab which exceeds that of the surrounding asthenosphere by three to five orders of magnitude (Fig. 3, 22.7–23.2 My). This situation poses a real challenge to the numerical method, which must be able to preserve the geometry of rigid falling objects in weak surroundings and not induce numerical diffusion of the thermal field during the rapid slab descent. As discussed by Gerya and Yuen [34], these strict numerical requirements can be successfully satisfied by using conservative finite differences and a marker-in-cell technique for solving the governing Eqs. (7)–(10).

Fig. 4 represents the free surface changes related to the breakoff process. In line with previously published data [8,18], slab detachment is followed by a period of uplift that reaches about 1.5 km within about 20 My. This uplift is mainly localized

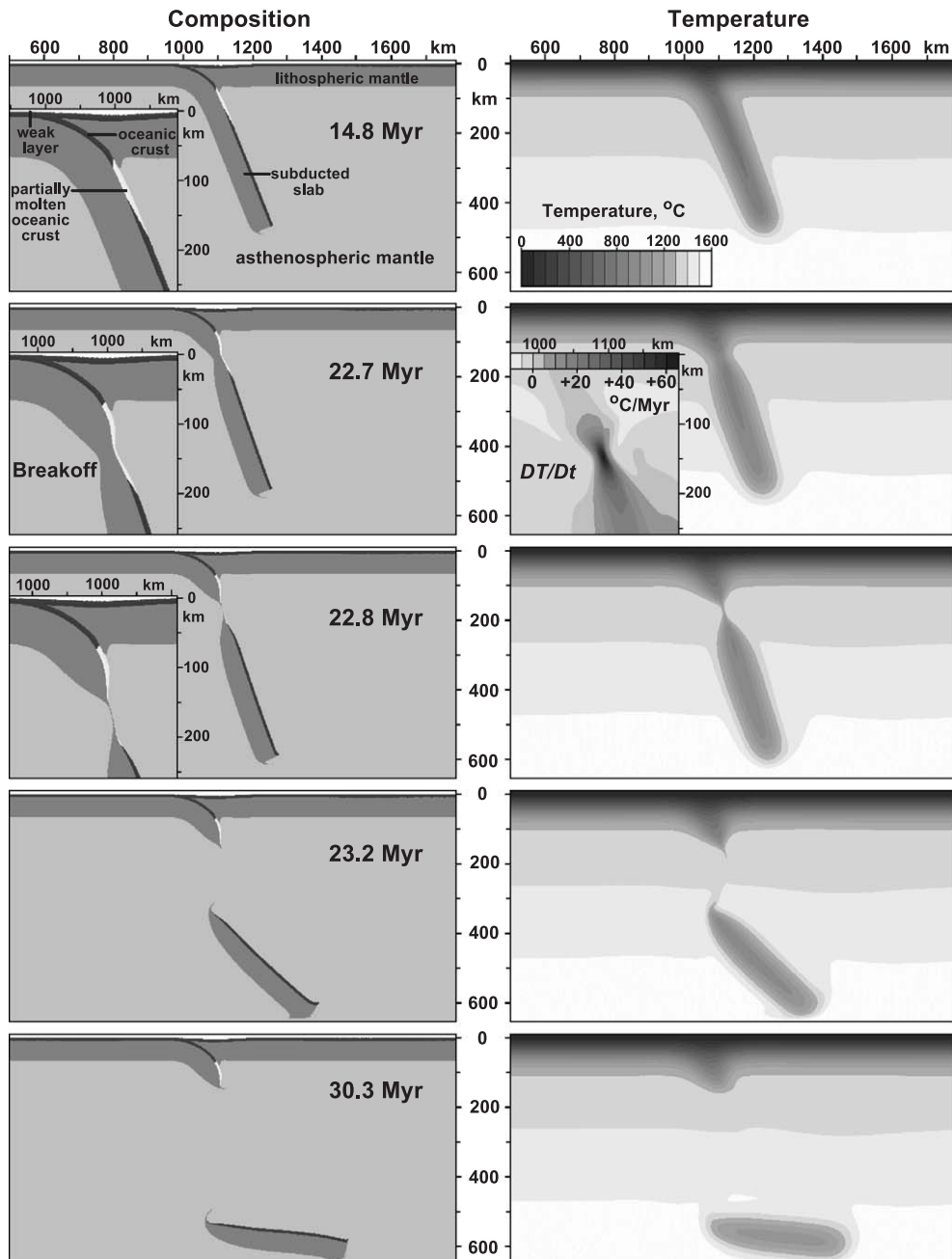


Fig. 2. Development of the geometry of the slab during ongoing detachment for reference model with cold slab (Model 1 in Table 2). Each sketch represents an enlarged 1300×660 km area of the original 2000×660 km models. Left: Evolution of the distribution of different rock types as indicated by markers. Right: Evolution of the temperature field. Zoomed area in the second row portrays the time of breakoff. Zoomed DT/Dt field (substantive time derivative) in the right column reflects focused thermal erosion of the slab due to shear heating.

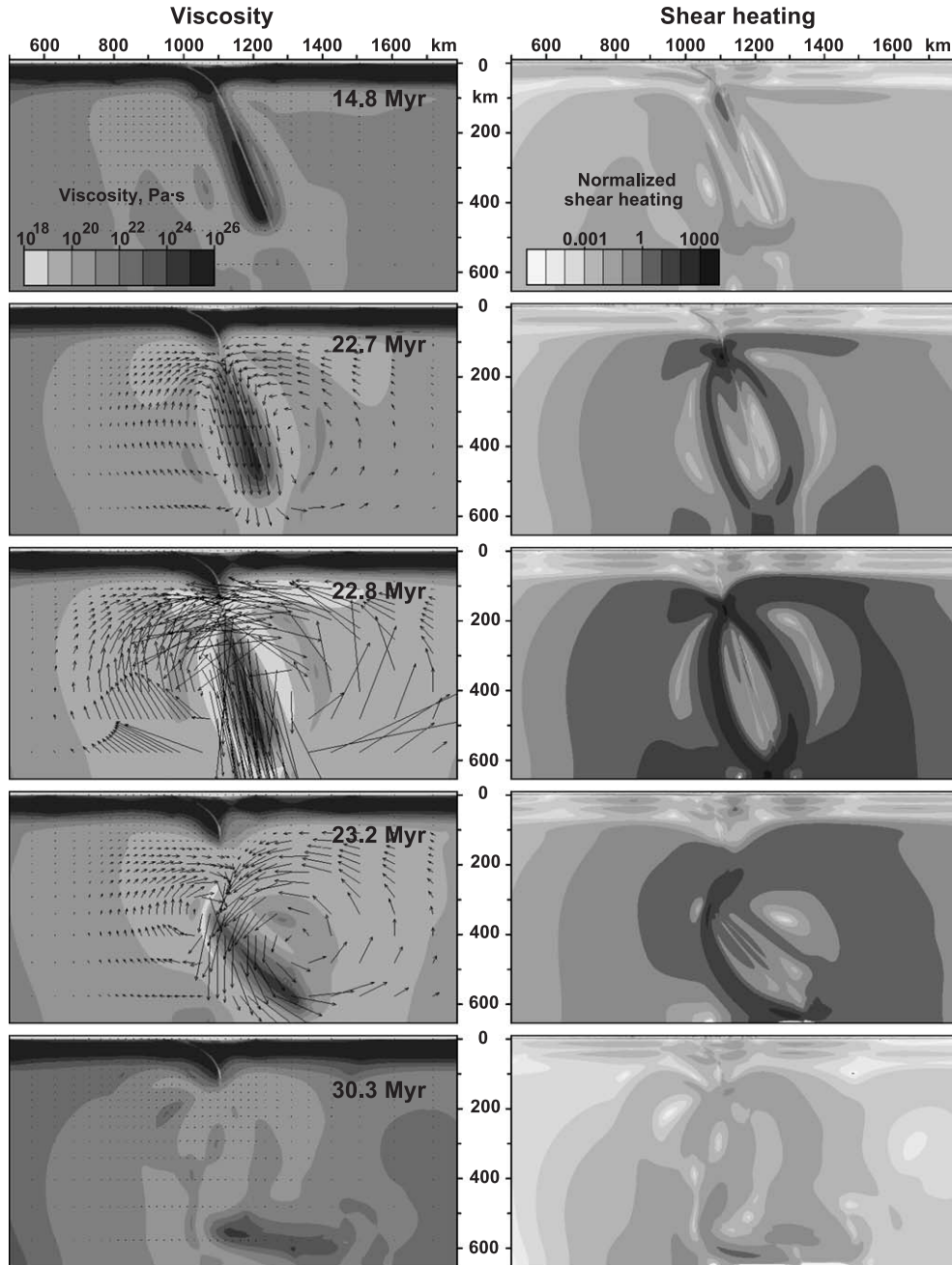


Fig. 3. Development of the viscosity field (left column) and distribution of shear heating (right column) of the model shown in Fig. 2. Arrows in the left column show the calculated velocity field. Shear heating has been normalized with respect to heating due to radioactive elements present in peridotite (Table 1). The second row represents the time of breakoff.

in a ~ 300 -km area within the overriding plate immediately above the detached slab. Initially the uplift area is characterized by a significant (~ 4.5 km)

depression developed during the initial period of slab bending and thermal diffusion. Since our model does not account for the lithospheric elasticity, the

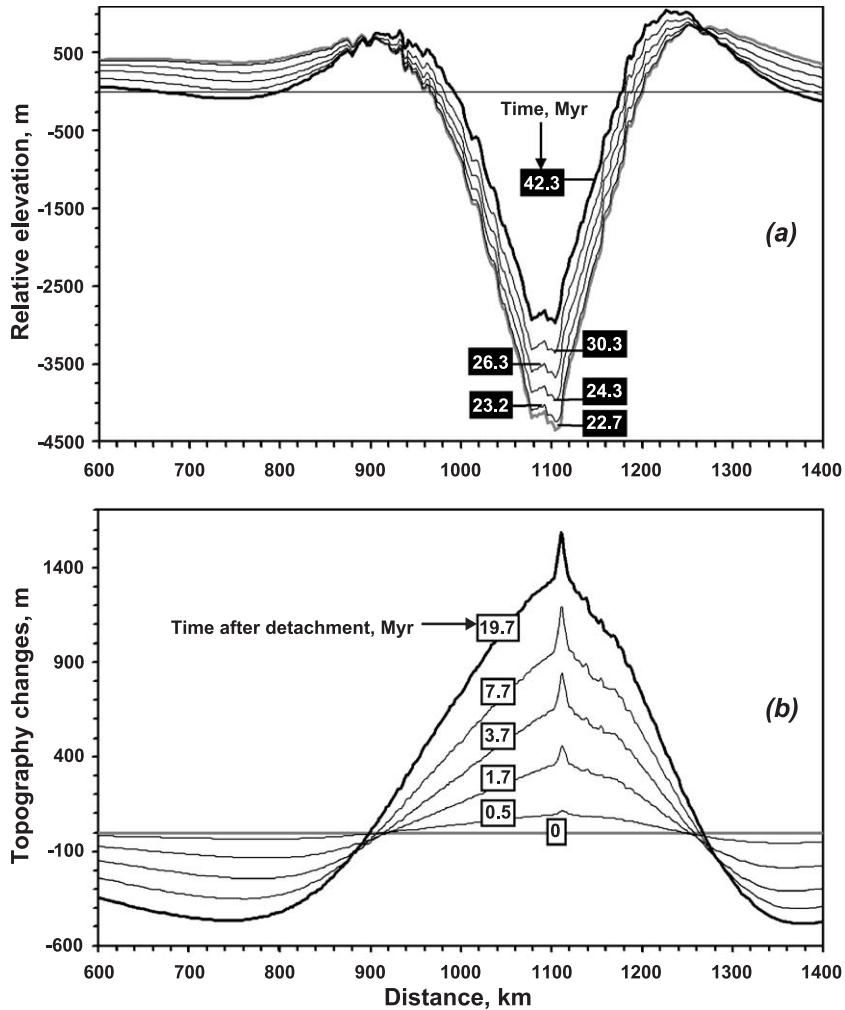


Fig. 4. Development of the free surface topography (a) and relative topography changes (b) calculated for the model shown in Fig. 2. The topography in (a) is calculated relative to the initial 8-km level. Topography changes in (b) are calculated by comparing the free surface topography at 22.7 Myr corresponding to the time of slab detachment (Fig. 2).

estimated uplift values are significantly lower than that estimated from elastic models (~ 6 km [18]) and needs further optimization by also accounting for the viscoelastic rheology of the rocks, erosion/sedimentation processes (e.g., [28,38]), and a more realistic geometry of the overriding plate that may include an accretion prism near the trench, as well as a volcanic arc and back-arc basin (e.g., [18]). Indeed, predicted initial uplift rates (0.4–0.8 km in 3.7 My, Fig. 4b) are similar to the values estimated by Rogers et al. [8] for the epeirogenic uplift above a detached slab in northern Central America (>1 km in >3.8 My).

Fig. 5 shows the results of numerical experiments for our second reference model, involving a warm slab (Model 11 in Table 2). In contrast to the previous model, detachment occurs much earlier at 13 My and at a much greater depth of ~ 400 km. This is obviously related to the initial temperature distribution, producing a lower position and a larger extent of necking area within the slab (cf. Fig. 5, 12.3 My and Fig. 2, 22.7 My). The detached fragment is much smaller and shows significant internal stretching before detachment (Fig. 5, 12.3 My). Indeed, this fragment also shows some degree

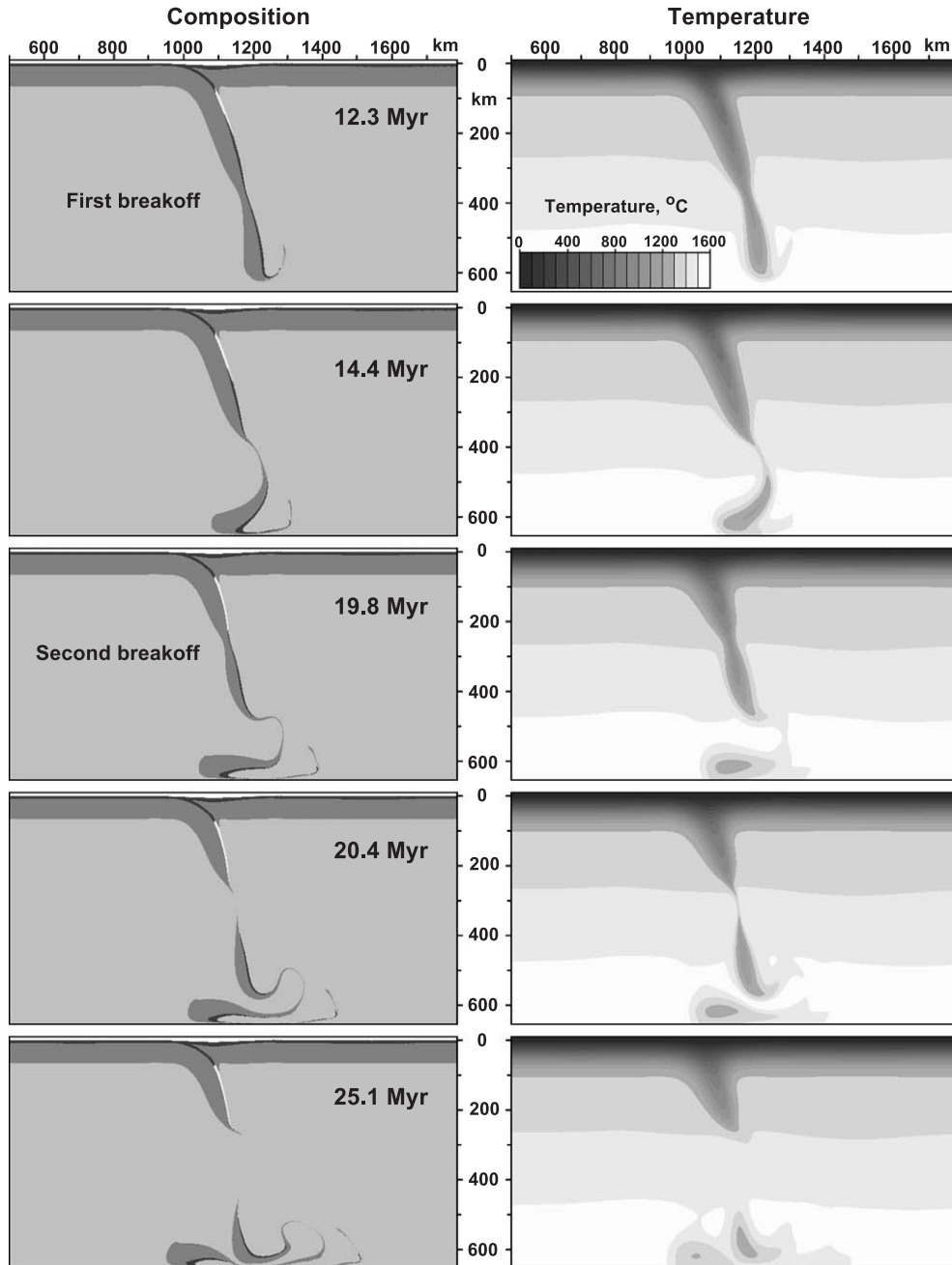


Fig. 5. Development of the geometry of the slab during ongoing detachment for reference model with warm slab (Model 11 in Table 2). Each sketch represents an enlarged 1300×660-km area of the original 2000×660-km models. We note that the slab breaks off twice. Left: Evolution of the distribution of rock types which show the slab geometry. Right: Evolution of the temperature field. Grey-scale code is the same as in Fig. 2.

of coherency, being rotated in proximity of the lower boundary (Fig. 5, 14.4 My). A unique feature of this model is the occurrence of a second slab detachment

episode at a later stage of ~20 My at a higher 270-km level within the slab. Intense stretching of the fragment and changes in geometry typical for a

Rayleigh–Taylor type process are direct consequences of the increased temperature, which is only 200–300 °C lower than the temperature of the surrounding asthenospheric mantle. Another important factor producing slab stretching is an increased density of the oceanic crust for this model (3500 kg m^{-3}), which mimics the consequence of the gabbro to eclogite transition (e.g., [23]). Interaction of different fragments produces complicated thermal structure at the bottom of the model, contrasting with the planar features obtained from experiments with a cold slab (cf. Fig. 2, 30.3. My, and Fig. 5, 25.1 My).

Table 2 displays a compilation of selected numerical experiments delineating the effect of variations in initial slab thermal structure, rock rheology, shear heating and melting. According to these data, the strong dependence of olivine rheology on pressure given by an effective activation volume of $16 \text{ J MPa}^{-1} \text{ mol}^{-1}$ [31] produces almost complete “freezing” of initial model geometry, because the

high effective viscosity of mantle exceeds 10^{22} Pa and precludes significant deformation on the time scale of the thermal diffusion of the slab (Model 4 in Table 2). Lowering of the effective activation volume results in a much earlier onset of detachment by comparison to the reference model, even for cold slabs (cf. Models 2 and 1 in Table 2). Taking into account that the activation energy for olivine creep decreases sharply with increasing water fugacity (e.g., [32,39]), the presence of water in the upper mantle [40] may be a major controlling factor for the onset of breakoff processes. The influence of a temperature- and pressure-dependent thermal conductivity (e.g., [35]) for the overall process of thermal heating of the slab is also significant [41,42]. An overall 20% increase in the thermal conductivity of rocks produces a ~20% acceleration of the onset of detachment (cf. Models 29 and 30 in Table 2), which is nonnegligible by current accuracy standards in geochronology.

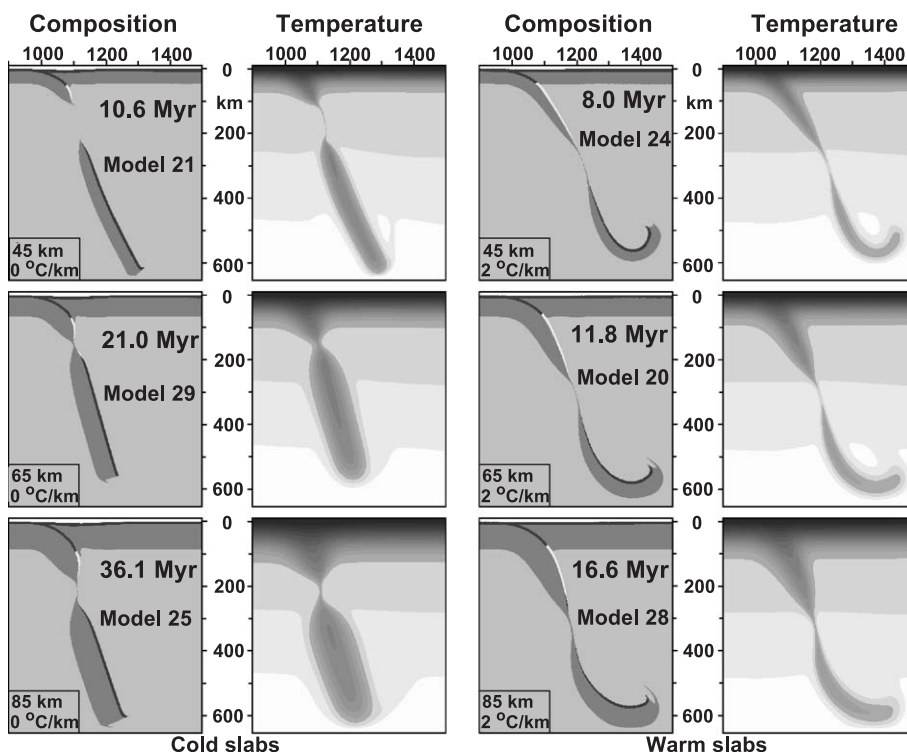


Fig. 6. Comparison of the geometry dependence of detachment for models with different initial thermal structure of the slab. Numbers in rectangles correspond to initial slab thickness (km) and initial longitudinal temperature gradient along the top of the slab (°C/km). The time given in the inset indicates the period of slab detachment. See Table 2 for other model parameters. Grey-scale code is the same as in Fig. 2.

Finally, Figs. 6 and 7 show the results of a systematic study of the depth and time of detachment as a function of the thermal parameters of the slab. We observe that the time of detachment correlates in an opposite sense with both the thickness of the slab and the longitudinal temperature gradient along the slab (Figs. 6 and 7a). These parameters can be related to the age and previous subduction rate (Table 2) of the

subducted slab. The depth of slab breakoff increases with an increasing longitudinal temperature gradient with a threshold at about 1 °C/km (Fig. 7b). This finding suggests that a bimodal nucleation of necking areas (at 100–150-km and at ~250-km depth) should exist along the slabs. In the case of warm slabs, this bimodal nucleation may result in the appearance of a second stage of slab detachment (Fig. 5, Table 2).

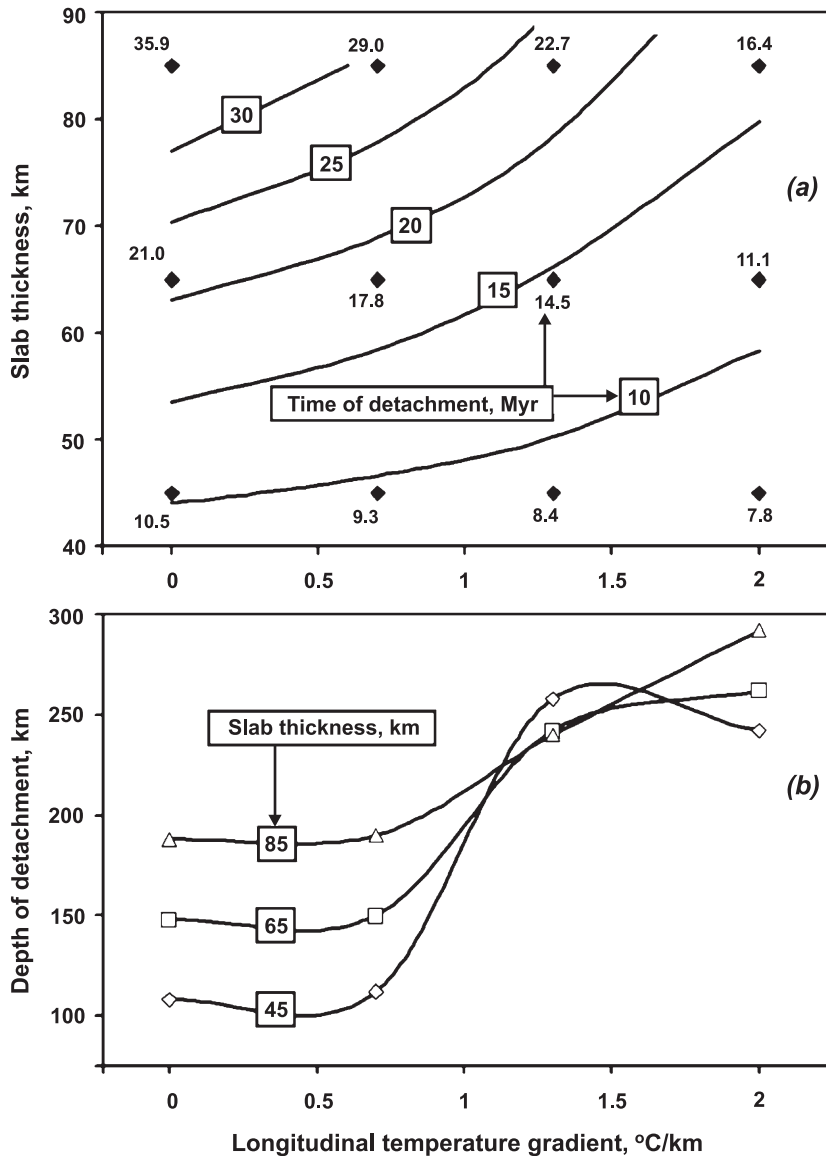


Fig. 7. Dependence of time (a) and depth (b) of detachment on the thermal structure of the slab. Results for Models 18 to 29 from Table 2 are used. Threshold in depths of detachment (b) suggests a bimodal (at 100–150-km and at ~250-km depth) distribution of slab necking areas nucleation (cf. Fig. 5). Numbers adjacent to different symbols in panel (a) indicate times for slab detachment.

7. Discussion, conclusions and perspectives

In this work, we have laid out the numerical setup for a realistic thermomechanical study of the slab detachment process. By dint of a wide parametric study, we have demonstrated the dynamic feasibility of the detachment process as caused by thermal diffusion of subducted slabs after cessation of active subduction. Our experiments show that this process can be initiated in form of slab necking, associated with partial melting of the subducted oceanic crust. The detachment process is accelerated due to the strain-rate softening and focusing of thermal erosion related to significant thermal feedback from shear heating. Slab detachment develops around 10% faster with viscous dissipation included, thus showing the potential importance of shear heating in this dynamic process. Inclusion of plasticity would act to accentuate the importance of shear heating due to a more nonlinear threshold phenomenon [43].

Our results on the initial thermal structure, thermal conductivity and effective rheology of the slab show that they play an influential role in the detachment process. The considerable influence of temperature- and pressure-dependent thermal conductivity supports the idea that the breakoff process is triggered by thermal diffusion with a time scale linearly dependent on the thermal conductivity. The degree of slab coherency defines a transition from (i) a typical slab breakoff+rapid coherent slab falling regime characteristic for cold slabs (previous subduction rate >6 cm/year, Table 2) to (ii) a Rayleigh–Taylor type process with rapid convective erosion of the slab from the bottom (e.g., [9]) characteristic for warm slabs with a previous subduction rate less than 4 cm/year (Table 2). A single detachment mode is characteristic for relatively cold and dense slabs (Table 2), producing large (hundreds of kilometers) fragments around 300–500 °C colder than the asthenosphere (Fig. 2, 30.3 My; Fig. 6, two left columns). Repetitive detachment (e.g., [7,29]) often develops in the case of relatively warm slabs characterized by significant lateral temperature gradients (Table 2), producing fragmentation of the slab to smaller objects (tens to hundreds of kilometers) that are 100–300 °C colder than the surrounding mantle (Fig. 5, 25.1 My; Fig. 6, two right columns). Rapid sinking and rotation of slab fragments may produce relatively cold areas lying

atop the lower mantle at the 660-km discontinuity, as inferred from seismic tomography data [5–7]. The thermal structure of these areas may be further complicated by 3-D rotations, internal deformation and interaction of the many different fragments (Fig. 5). Regular planar tomographic features will only be formed in the case of extremely cold and large fragments of slabs, thus preserving much internal coherency after the detachment (Fig. 2).

Extrapolating our 2-D results, we can conclude that instead of being considered as planar (e.g., [4,14,15]) or wedge-like tears [5], the three-dimensional geometry of the detachment process should rather have the form of laterally propagating necking of the slab (Fig. 8). Initiation of necking will strongly depend on the initial thermomechanical structure of the slab and may lead to the development of either asymmetric [5] or relatively symmetric (Fig. 8) breakoff structures. In the absence of weak zones inside slab, necking should propagate away from the slab margins (Fig. 8) where thermal diffusion is most significant. On the other hand, due to the presence of initial slab nonhomogeneity, necking structures may start either from the margins or within the core of the plate, giving significant variations in breakoff geometry and dynamics. Rapid changes in topography and significant volcanic activity, particularly accompanied by singular types of volcanic rocks due to the melting of

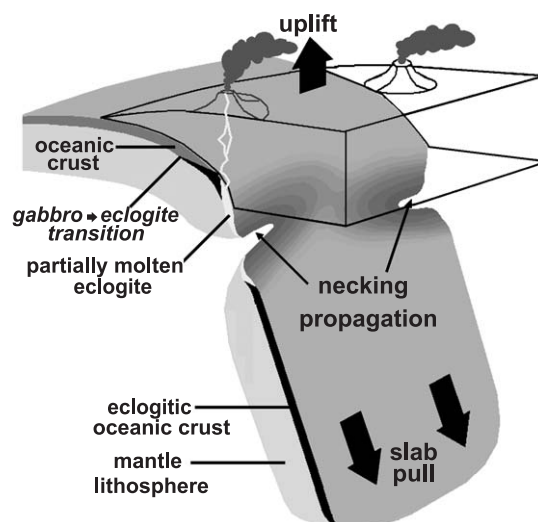


Fig. 8. Conceptual 3-D model of the slab breakoff geometry inferred from our 2-D numerical experiments. See the text for discussion.

subducted oceanic crust, are plausible consequences of this geodynamic scenario (Fig. 8).

Future directions in the modeling of slab detachment will include dynamic cases with more complicated starting geometries and thermal structures of slabs matching initiation of continental collision; the study of the effects of phase transformations within the crust and the mantle (e.g., [44]); and the influence of slab viscoelasticity and the accompanying rapid snap-off process due to a finite yield strength [43]. We note that the presence of viscoelasticity in the slab bending region may potentially store an abundant amount of elastic potential energy, which can be converted into localized shear heating [45] (Kaus and Podladchikov, manuscript in preparation) in the slab necking area, thus accelerating the slab detachment.

Acknowledgements

This work was supported by ETH Research Grant TH-12/04-1, by RFBR grants #03-05-64633 and #1645-2003-5, by an Alexander von Humboldt Foundation Research Fellowship to TVG, by the geophysics program of the National Science Foundation and by the German Science Foundation within SFB 526. Arne P. Willner, Klaus Regenauer-Lieb and Anne M. Hofmeister are thanked for discussions and comments. Constructive reviews by G.A. Houseman and an anonymous reviewer are appreciated.

References

- [1] B. Isacks, P. Molnar, Mantle earthquake mechanisms and the sinking of the lithosphere, *Nature* 223 (1969) 1121–1124.
- [2] P.E. Sacks, D.T. Secor, Delamination in collisional orogens, *Geology* 18 (1990) 999–1002.
- [3] F. Von Blanckenburg, J.H. Davies, Slab breakoff: a model for syncollisional magmatism and tectonics in the Alps, *Tectonics* 14 (1995) 120–131.
- [4] J.H. Davies, F. Von Blanckenburg, Slab breakoff: a model of lithospheric detachment and its test in the magmatism and deformation of collisional orogens, *Earth Planet. Sci. Lett.* 129 (1995) 85–102.
- [5] M.J.R. Wortel, W. Spakman, Subduction and slab detachment in the Mediterranean–Carpathian region, *Science* 290 (2000) 1910–1917.
- [6] P.F. Xu, R.M. Sun, F.T. Liu, Q. Wang, B. Cong, Seismic tomography showing, subduction and slab breakoff of the Yangtze block beneath the Dabie–Sulu orogenic belt, *Chin. Sci. Bull.* 45 (2000) 70–74.
- [7] V. Levin, N. Shapiro, J. Park, M. Ritzwoller, Seismic evidence for catastrophic slab loss beneath Kamchatka, *Nature* 418 (2002) 763–767.
- [8] R.D. Rogers, H. Káráson, R.D. van der Hilst, Epeirogenic uplift above a detached slab in northern Central America, *Geology* 30 (2002) 1031–1034.
- [9] R.N. Pysklywec, C. Beaumont, P. Fullsack, Modeling the behavior of the continental mantle lithosphere during plate convergence, *Geology* 28 (2000) 655–658.
- [10] A.T. Ismail-Zadeh, V.I. Kellis-Borok, A.A. Soloviev, Numerical modelling of earthquake flows in the southeastern Carpathians (Vrancea): effects of a sinking slab, *Phys. Earth Planet. Inter.* 111 (1999) 267–274.
- [11] A.T. Ismail-Zadeh, G.F. Panza, B.M. Naimark, Stress in the descending relic slab beneath the Vrancea region, Romania, *Pure Appl. Geophys.* 157 (2000) 111–130.
- [12] F. Wenzel, F.P. Lorenz, B. Spemer, M.C. Oncescu, Seismotectonics of the Romanian Vrancea area, in: F. Wenzel, D. Lingu, O. Novak (Eds.), *Vrancea Earthquakes: Tectonics, Hazard and Risk Mitigation*, Kluwer, Dordrecht, (1999), pp. 15–25.
- [13] S.Y.M. Wong A Ton, M.J.R. Wortel, Slab detachment in continental collision zones: an analysis of controlling parameters, *Geophys. Res. Lett.* 24 (1997) 2095–2098.
- [14] S. Yoshioka, M.J.R. Wortel, Three-dimensional numerical modeling of detachment of subducted lithosphere, *J. Geophys. Res.* 100 (1995) 20233–20244.
- [15] S. Yoshioka, D.A. Yuen, T.B. Larsen, Slab weakening: thermal and mechanical consequences for slab detachment, *Island Arc* 40 (1995) 89–103.
- [16] G.A. Houseman, D. Gubbins, Deformation of subducted oceanic lithosphere, *Geophys. J. Int.* 131 (1997) 535–551.
- [17] T.B. Larsen, D.A. Yuen, A.V. Malevsky, Dynamical consequences on fast subducting slabs from a self-regulating mechanism due to viscous heating in variable viscosity convection, *Geophys. Res. Lett.* 22 (1995) 1277–1280.
- [18] S.J.H. Buiters, R. Govers, M.J.R. Wortel, Two-dimensional simulations of surface deformation caused by slab detachment, *Tectonophysics* 354 (2002) 195–210.
- [19] B. Schott, D.A. Yuen, H. Schmeling, The significance of shear heating in continental delamination, *Phys. Earth Planet. Inter.* 110 (2000) 273–290.
- [20] D.L. Turcotte, G. Schubert, *Geodynamics: Applications of Continuum Physics to Geological problems*, John Wiley, New York, 1982, 430 pp.
- [21] D. Bittner, H. Schmeling, Numerical modeling of melting processes and induced diapirism in the lower crust, *Geophys. J. Int.* 123 (1995) 59–70.
- [22] C. Clauser, E. Huenges, Thermal conductivity of rocks and minerals, in: T.J. Ahrens (Ed.), *Rock Physics and Phase Relations*, AGU Reference Shelf 3, AGU, Washington DC, 1995, pp. 105–126.
- [23] M.W. Schmidt, S. Poli, Experimentally based water budgets for dehydrating slabs and consequences for arc magma generation, *Earth Planet. Sci. Lett.* 163 (1998) 361–379.

- [24] D.P. McKenzie, Speculations on the consequences and causes of plate motions, *Geophys. J. R. Astron. Soc.* 18 (1969) 1–32.
- [25] B. Schott, H. Schmeling, Delamination and detachment of a lithospheric root, *Tectonophysics* 296 (1998) 225–247.
- [26] A.P. Willner, E. Sebazungu, T.V. Gerya, W.V. Maresch, A. Krohe, Numerical modelling of PT-paths related to rapid exhumation of high-pressure rocks from the crustal root in the Variscan Erzgebirge Dome (Saxony/Germany), *J. Geodyn.* 33 (2002) 281–314.
- [27] G. Schubert, D.A. Yuen, D.L. Turcotte, Role of phase transitions in a dynamic mantle, *Geophys. J. R. Astron. Soc.* 42 (1975) 705–735.
- [28] T.V. Gerya, D.A. Yuen, Rayleigh–Taylor instabilities from hydration and melting propel “cold Plumes” at subduction zones, *Earth Planet. Sci. Lett.* 212 (2003) 47–62.
- [29] M.R. Haschke, E. Scheuber, A. Günther, K.-J. Reutter, Evolutionary cycles during the Andean orogeny: repeated slab breakoff and flat subduction? *Terra Nova* 14 (2002) 49–55.
- [30] A. Nicolas, *The Mid-Oceanic Ridges: Mountains Below Sea Level*, Springer Verlag, Berlin, 1995, 200 pp.
- [31] G. Ranalli, *Rheology of the Earth*, 2nd ed., Chapman & Hall, London, 1995, 413 pp.
- [32] S. Mei, D.L. Kohlstedt, Influence of water on plastic deformation of olivine aggregates, *J. Geophys. Res.* 105 (2000) 21457–21481.
- [33] W.F. Brace, D.L. Kohlstedt, Limits on lithospheric stress imposed by laboratory experiments, *J. Geophys. Res.* 85 (1980) 6248–6252.
- [34] T.V. Gerya, D.A. Yuen, Characteristics-based marker-in-cell method with conservative finite-differences schemes for modeling geological flows with strongly variable transport properties, *Phys. Earth Planet. Inter.* 140 (2003) 295–320.
- [35] A.M. Hofmeister, Mantle values of thermal conductivity and the geotherm from phonon lifetimes, *Science* 283 (1999) 1699–1706.
- [36] M.L. Rudolph, T.V. Gerya, D.A. Yuen, S. DeRosier, Visualization of multiscale dynamics of hydrous cold plumes at subduction zones, *Vis. Geosci.* 8 (2004) doi:10.1007/510069-004-0017-2.
- [37] T.B. Larsen, D.A. Yuen, J.J. Smedsmo, A.V. Malevsky, Generation of fast time scale phenomena in thermo-mechanical processes, *Phys. Earth Planet. Inter.* 102 (1997) 213–222.
- [38] S. Lamb, P. Davis, Cenozoic climate changes as a possible cause of the rise of the Andes, *Nature* 425 (2003) 792–797.
- [39] H. Jung, S.I. Karato, Effects of water on dynamically recrystallized grain-size of olivine, *J. Struct. Geol.* 23 (2001) 1337–1344.
- [40] K. Regenauer-Lieb, D.A. Yuen, J. Branlund, The initiation of subduction: critically by addition of water? *Science* 294 (2001) 578–580.
- [41] S.A. Hauck, R.J. Phillips, A.M. Hofmeister, Variable conductivity: effects on the thermal structure of subducting slabs, *Geophys. Res. Lett.* 26 (1999) 3257–3260.
- [42] L. Starin, D.A. Yuen, S.Y. Bergeron, Thermal evolution of sedimentary basin formation with temperature-dependent conductivity, *Geophys. Res. Lett.* 27 (2000) 265–268.
- [43] K. Regenauer-Lieb, D.A. Yuen, Modeling shear zones in geological and planetary sciences: solid- and fluid-thermal-mechanical approaches, *Earth-Sci. Rev.* 63 (2003) 295–349.
- [44] D. Brunet, P. Machel, D.A. Yuen, Slab weakening by the exothermic olivine-spinel phase change, *Geophys. Res. Lett.* 25 (1998) 3231–3234.
- [45] K. Regenauer-Lieb, D.A. Yuen, Rapid conversion of elastic energy into plastic shear heating during incipient necking of the lithosphere, *Geophys. Res. Lett.* 25 (1998) 2737–2740.